RSC Advances

Check for updates

Defect and carrier characteristics of chalcogenide perovskite BaZrS₃ under thermodynamic stability: a first-principles study for photovoltaic application

Qinmiao Chen, [ID] *[a] Yi Ni[a] and Yufei Wang[bc]

BaZrS₃ is reported to be an exceptional chalcopyrite perovskite with remarkable stability, making it a key material for the next-generation perovskite-inspired technologies. In this study, the thermodynamic stability of BaZrS₃ was investigated while referencing all potential secondary phases in the Materials Project database. Furthermore, the influence of element doping on both the bands and thermodynamic stability of BaZrS₃ was also studied, the band adjustment efficiency was validated, and experimental synthesis challenges were elucidated. Based on a large supercell, Heyd–Scuseria–Ernzerhof hybrid functional and finite-size effect correction, the concentration properties of defects and charge carriers of BaZrS₃ were then determined in the thermodynamically stable region, from the characteristics of defect formation energy with varied Fermi levels. The results indicate that degenerated semiconductor characteristics exist in BaZrS₃ in the thermodynamically stable region, which should be avoided. The defect transition energy level characteristics of BaZrS₃ were also calculated and identified. Additionally, the properties of deep-level defects S_i with high concentration were analyzed. While S_i (+2/0) exhibits deep-level defect states, S_i (+1/0) does not. The non-radiative and radiative capture coefficients of deep-level defect S_i (+2/0) were calculated at 1.28682×10^{-25} and 3.51×10^{-15} cm³ s⁻¹, respectively. The obtained defect and carrier qualities of BaZrS₃ were applied to evaluate its photoelectric conversion efficiency. The manuscript investigates, for the first time, how defects evolve with changes in chemical potential in stable BaZrS₃, providing valuable guidance for the experimentally controllable preparation of high-quality BaZrS₃ films or devices.

1 Introduction

Perovskite materials have been the subject of a lot of research over the past decade and have been gaining prominence in the fields of photovoltaic,[1–5] photodetection[6–8] and light-emitting applications.[9–11] In recent years, halides have made up the majority of the semiconductor perovskite materials that have been thoroughly studied. Halide perovskites exhibit synergistically reduced band gaps suitable for photovoltaic applications, which can be attributed to the low conduction band resulting from the strong spin–orbit coupling in cations, such as lead, and the high valence band contributed by anions, such as the iodine 6p orbitals.[12,13] Another crucial physical property of halide perovskites is the defect tolerance, which allows these materials to be readily prepared for device fabrication with less need for high purity and high crystallinity, while keeping

production costs low. Currently, halide perovskites face two main obstacles to larger-scale deployment: (i) long-term stability problems, partially due to the inherent instability of their organic components against moisture, heat, light and electric fields; and (ii) toxicity, primarily arising from the use of lead.[14–17] These drawbacks have severely impeded their commercial application.

Since their initial synthesis in 1957,[18] chalcogenide perovskites (CPs with the formula ABX₃; A, B = metals with a combined valence of 6; X = S, Se or other chalcogen elements) have demonstrated the anticipated benefits of outstanding thermal and aqueous stability in addition to their nontoxic elemental composition. Although many CPs have been documented since then, research on their physical characteristics has remained intermittent.[19–21] Inspired by the success of halide perovskites, CPs have been proposed for photovoltaic applications in recent years. Their tunable band gaps (in the range 0.5 to 2.2 eV), strong light absorption coefficients (at 10^{-5} cm⁻¹), small effective masses of charge carriers (m_e, m_h < 1) and superior environmental stability in comparison to halide perovskites have made them promising candidates for next-generation optoelectronic devices.[22–27] Among these, barium zirconium sulfide (BaZrS₃) is notable for its ideal direct band

[a]School of Physics, East China University of Science and Technology, 130 Meilong Road, Shanghai 200237, China. E-mail: qmchen@ecust.edu.cn

[b]Laboratory of Solid State Optoelectronics Information Technology, Institute of Semiconductors, Chinese Academy of Sciences, Beijing 100083, China

[c]College of Future Technology, University of Chinese Academy of Sciences, Beijing 101408, China

gap (1.7 to 1.9 eV),excellent dielectric response and defect tolerance.[23,24,28–34] Additionally, $BaZrS_3$ is found to exist preferentially in the distorted perovskite phase with 3D-connected corner-sharing BX_6 octahedra.[35] While other chalcogenide perovskites preferentially form phases with either edge-sharing or isolated BX_6 octahedra (so-called "needle-like"[36,37] and "hexagonal" phases[38,39]). Because of the absence of connected octahedra along certain directions of the crystal structure, these structures are predicted to show more localized conduction and valence band edges, which will result in heavy electron and hole masses. Consequently, $BaZrS_3$ is anticipated to be more appropriate for optoelectronic devices from the perspective of carrier mobility. As a result, $BaZrS_3$ is a preferred material to evaluate whether CPs are viable options for applications to optoelectronic devices both theoretically and experimentally. For optoelectronic materials, one of the most important properties is their carrier concentration. A high carrier concentration is essential for achieving a high short-circuit current.[40–42] However, the carrier concentration of CPs, including $BaZrS_3$, has been scarcely reported in the literature, especially under thermodynamically stable conditions. Another crucial aspect for exceptional photoelectric materials is their defect characteristics, which affect the total performance of manufactured devices like solar cells. For example, the open-voltage, short-circuit current and fill factor of the solar cells are directly related to how many charge carriers can ultimately be transferred to the external circuit after carrier recombination by defects.[43] In optoelectronic materials, recombination centers (RCs), which typically manifest as deep-level defects, should be avoided as they compete with the desired carriers. It has been demonstrated that intrinsic defects in halide perovskites are mostly shallow defects, which do not serve as effective RCs.[42,44–48] This characteristic enables low-cost material synthesis and low-cost device fabrication without requiring complex defect management. Defect tolerance has been identified as one of the special qualities of halide perovskites in terms of their achievements,[43,44,49–51] allowing for effective solar cell performance even in the presence of high defect concentration. Then, what are the characteristics of defects in $BaZrS_3$?

According to recent hybrid density functional theory (DFT) computational investigations conducted by Sunfs group, $BaZrS_3$ has a distinct self-passivation process in which the majority of vacancies and antisite defects generate shallow transition levels, as opposed to deep-level RCs. Although it has been claimed that several types of defects, such as S_i and S_{Ba}, are deep-level defects. It is supposed that, for deep-level defects including S_i and S_{Ba}, the formation of S clusters (dimer, trimer and tetramer) tends to remove mid-gap states in the neutral charge state and leaves behind a relatively clean band gap.[29] They also conducted calculations with the PBEsol + U functional, and the results show that the intrinsic defects of $BaZrS_3$ are all shallow-level defects, despite the underestimated band gap. In addition, Yan's group also studied the defect transition levels of $BaZrS_3$ with the GGA + U functional.[22] Comparison of the findings from these investigations, however, shows they have very different defect transition characteristics, particularly for the locations of deep-level defects in the band gap.[22,29]

Experimental validations also highlight discrepancies and synthesis-dependent defect kinetics. Compared to epitaxial thin films or single crystals, solution-synthesized $BaZrS_3$ nanoparticles exhibit larger defect concentrations, resulting in reduced carrier lifetime.[30,34,52] Therefore, such findings highlight the need to bridge theoretical defect characteristics with practical synthesis protocols, using a better understanding of the defect characteristics of $BaZrS_3$ under thermodynamic stability. However, the quantitative data that can adequately support the defect characteristics of $BaZrS_3$ is currently missing.

In this study, based on a large nearly cubic supercell of 240 atoms, the Materials Project database, the Vienna *Ab initio* Simulation Package (VASP) and the Defect and Dopant *Ab initio* Simulation Package (DASP),[53–56] the optical properties and thermodynamic stability of $BaZrS_3$ were studied first. The chemical potential of the stable $BaZrS_3$ compound was determined while fully considering the competitive secondary phases. Then, the defect formation energy, ionization energy, carrier concentration, Fermi energy level and deep-level defects, along with the non-radiation/radiation recombination characteristics of $BaZrS_3$, were systematically investigated in the thermodynamically stable region. Finally, the quantitative defect and carrier characteristics of $BaZrS_3$ were obtained, and their effects on the photoelectric properties of $BaZrS_3$ were examined.

2 Method of calculation

The electronic structure of the orthorhombic chalcogenide perovskite $BaZrS_3$ (*pnma*, NO. 62) was examined in the study by first-principles calculations, as mentioned above. The total energy calculations were performed in VASP using density functional theory with *a* plane wave energy cutoff of 336 eV (about 1.3 times the ENMAX in the pseudopotential files in the projector-augmented wave (PAW) method).[57,58] To determine the stable chemical potential range, the structures (along with the reciprocal space meshes) and PAW potentials (GGA-PBE) of the elemental components and secondary phases were all taken from the data provided in the Materials Project database. At first, the relaxation of the structure was done at the PBE level to obtain a converged WAVECAR file, and then the calculations were performed using the Heyd–Scuseria–Ernzerhof hybrid functional (HSE06) with the converged WAVECAR. The defect characteristics of $BaZrS_3$ were studied using a large supercell of 240 atoms with a nearly cubic structure. The Γ point was used to represent the Brillouin zone. The PAW potentials for $BaZrS_3$ were kept the same. The forces were fully relaxed to below 0.01 eV Å^{-1}, and defect corrections (including potential alignment for charged defects) were performed.[59] HSE06 and finite-size electrostatic correction schemes were employed to determine the formation energy and transition energy levels of the defects.[60–62] The band gap of $BaZrS_3$ was fixed at a value of 1.732 eV, with a Hartree–Fock exchange value α of about 0.2163.

For $BaZrS_3$, the considered intrinsic defects in this study include the Ba, Zr and S vacancies (V_{Ba}, V_{Zr} and V_S), interstitials (Ba_i, Zr_i and S_i) and antisites (Ba_{Zr}, Ba_S, Zr_{Ba}, Zr_S, S_{Ba} and S_{Zr}).

Taking S vacancies in the charge state q as an example, its defect formation energy $\Delta E_f(V_S^q)$ can be calculated from eqn (a):[63–65]

$$\Delta E_f(V_S^q) = E(V_S^q) - E(\text{bulk}) + E(S) + \mu_S + q(E_F + E_{VBM}) + E_{corr} \tag{a}$$

where the total energy of the supercell with and without an S vacancy is denoted by $E(V_S^q)$ and $E(\text{bulk})$. μ_S is the elemental chemical potential of S referenced to its total energy $E(S)$. E_F is the Fermi level referenced to the eigenvalue of the valence band maximum (VBM) level of the bulk defect-free supercell of BaZrS$_3$. E_{corr} is the correction for charged defects to account for the finite-size effect, with the FNV (Freysoldt–Neugebauer–Van de Walle) method.[62] The formation energy of V_S in BaZrS$_3$ was calculated in the supercell structure, as mentioned above. The charge transition level is equal to the Fermi-level position, where the formation energies in two charge states are the same. For neutral and 1+ charge states, the $\alpha(0/1+)$ charge transition level with respect to the VBM ($E_F = 0$) can be calculated with eqn (b):

$$\alpha(0/1+) = \Delta E_f(V_S^0; E_F = 0) - \Delta E_f(V_S^+; E_F = 0) \tag{b}$$

For the calculation of the non-radiative recombination characteristics of deep-level defects with high concentration, the excited-state carrier dynamics properties based on the phonon spectrum and electron–phonon coupling were studied. As an example, the hole capture coefficient C_p by V_S^0 can be calculated using the one-dimensional static coupling approximation, as in eqn (c):[66]

$$C_p = \frac{2\pi V}{\hbar} W_{if}^2 \sum_m \omega_m \sum_n \langle \chi_{im}|\Delta Q|\chi_{fn}^2 \rangle \delta(\Delta E + E_{im} - E_{fn}) \tag{c}$$

where the electron–phonon coupling matrix element W_{if} was determined using VASP via bulk/single-particle wave functions under related approximations, methods and theories in ref. 66 and 67. ω_m is the thermal occupation of the initial vibrational state m, χ_{im} and χ_{fn} are the vibrational wave functions and E_{im} and E_{fn} are the related eigenvalues. ΔQ is the difference in the equilibrium geometries of the initial and final state along the configuration coordinate. The carrier transition energy was denoted by ΔE; for the case of hole capture by V_S^0, ΔE is exactly the same as the $\alpha(0/1+)$ transition level. More details of the element or parameter calculation in eqn (e) for carrier capture can be found in ref. 66 and 67, as indicated above.

3 Results and discussion

3.1 Optical characteristics of BaZrS$_3$

The optical characteristics of BaZrS$_3$ were investigated using standard DFT calculations with the HSE06 hybrid functional. First-principles calculations reveal the distinctive optical characteristics of BaZrS$_3$, as displayed in Fig. S1(a). The optical absorption spectrum exhibits three prominent peaks at 2.25, 2.57 and 3.87 eV, which could be assigned to direct allowed transitions between hybridized Zr-d and S-p orbitals.[68] The absorption coefficient exceeds 10^5 cm^{-1} near the band edge,[68] demonstrating light-harvesting capabilities on a par with or

even better than those of CH$_3$NH$_3$PbI$_3$ and GaAs (at 10^4 cm^{-1}),[2] and significantly higher than that of silicon.[69] The calculated characteristic curve is generally consistent with that from experimental-quality BaZrS$_3$ thin films.[23] The optical absorption edge of BaZrS$_3$ is at 1.96 eV from optical calculation, as indicated by the tangent in Fig. S1(a). Furthermore, the remarkable light-harvesting ability of BaZrS$_3$ single crystals at 10^6 cm^{-1} has also been asserted,[34] suggesting their potential as superior optoelectronic materials.

Fig. S1(b) illustrates the dielectric response properties of BaZrS$_3$. The real component exhibits a characteristic dispersion with a static dielectric constant of 10.2, in good agreement with earlier hybrid functional predictions.[29] The dielectric constant of BaZrS$_3$ is a little lower than that of silicon (11.7)[70] and GaAs (12.88) but higher than that of CH$_3$NH$_3$PbI$_3$ (6.5).[71] The imaginary part onset at 1.91 eV, as displayed in the inset to Fig. S1(b), coincides with the absorption edge in Fig. S1(a).

3.2 Thermodynamic stability of BaZrS$_3$

The stability of BaZrS$_3$ is a prerequisite for studying its properties. During the crystal growth of BaZrS$_3$, although the abundance of a certain element can be controlled by changing the environment, the changes in the elemental chemical potentials are not actually unlimited, because they should satisfy a series of thermodynamic conditions to make the pure-phase crystalline semiconductor stable. Under equilibrium growth conditions, the weighted sum of the chemical potentials of its component elements should be equal to the formation energy of BaZrS$_3$, as illustrated in eqn (d). Here μ_i is the chemical potential of the element, where i refers to the most stable phase of the involved elements. The elemental chemical potentials are referenced to uncorrected DFT energies at 0 K. μ_{BaZrS_3} represents the formation energy of BaZrS$_3$ that can be calculated from the total energy of BaZrS$_3$ and the elemental standard states. Additionally, to ensure that the synthesized sample is pure-phase BaZrS$_3$, the formation or coexistence of the competing secondary phases, such as the binary and ternary compounds ZrS$_2$, ZrS$_3$, Zr$_3$S$_4$ and Ba$_3$Zr$_2$S$_7$, and the elemental phases Cu, Zr, S, should be avoided. Therefore, the weighted sum of the chemical potentials of their component elements should be lower than their corresponding formation energies (the formation energies of elemental phases are 0). As a result, the relationships in eqn (e) must also be satisfied, as detailed in the equations below. Here μ_{ZrS_2}, μ_{ZrS_3}, $\mu_{Zr_3S_4}$ and $\mu_{Ba_3Zr_2S_7}$ represent the formation energies of ZrS$_2$, ZrS$_3$, Zr$_3$S$_4$ and Ba$_3$Zr$_2$S$_7$, respectively, which can also be calculated from the total energy of ZrS$_2$, ZrS$_3$, Zr$_3$S$_4$ and Ba$_3$Zr$_2$S$_7$, and the elemental standard states.

$$\mu_{Ba} + \mu_{Zr} + 3\mu_S = \mu_{BaZrS_3} = -9.9535 \text{ eV} \tag{d}$$

$$\mu_{Zr} + 2\mu_S < \mu_{ZrS_2} = -5.1287 \text{ eV}, \quad \mu_{Zr} + 3\mu_S < \mu_{ZrS_3}$$
$$= -5.4155 \text{ eV}, \quad 3\mu_{Zr} + 4\mu_S < \mu_{Zr_3S_4}$$
$$= -12.1999 \text{ eV}, \quad 3\mu_{Ba} + 2\mu_{Zr}$$
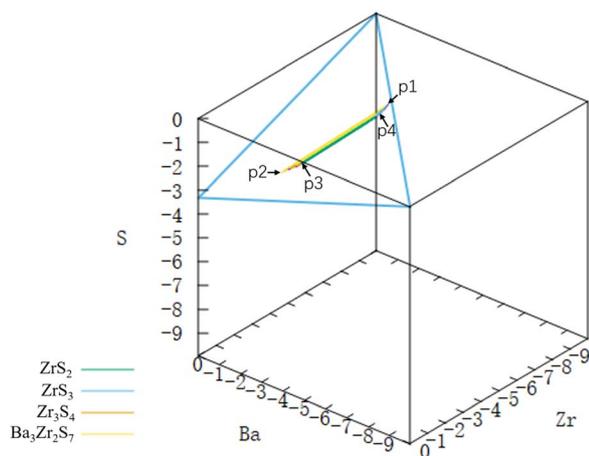$$+ 7\mu_S < \mu_{Ba_3Zr_2S_7} = -24.4885 \text{ eV}. \tag{e}$$

Fig. 1 The calculated chemical potential region where $BaZrS_3$ is stable against the formation of three constituent elements and four competitive compounds (*i.e.*, the allowed chemical potential region is bounded by $Ba_3Zr_2S_7$, Zr_3S_4, ZrS_3 and ZrS_2).

As discussed above, the three constituent elements, Ba, Zr, S, and four additional compounds, ZrS_2, ZrS_3, Zr_3S_4 and $Ba_3Zr_2S_7$, are considered competitive secondary phases of $BaZrS_3$. (It should be noted that, when $\mu_{Ba} = 0$, $\mu_{Zr} = 0$ and $\mu_S = 0$, it means that these elements are so rich that their pure solid phase can be formed). Under these constraints, according to the calculations, the chemical potential range of Ba, Zr and S that stabilizes the $BaZrS_3$ compound is bound to a polyhedron in the μ_{Ba}, μ_{Zr} and μ_S space, as depicted in Fig. 1. Table 1 lists the chemical potential boundary points p1–p4 that correspond to Fig. 1. As indicated in Table 1, we focus the discussion in the following sections on the stable region of $BaZrS_3$ with boundary points p1–p4.

Researchers additionally investigated the features of $BaZrS_3$ doped by Ti or Se to lower its band gap to an ideal value of around 1.34 eV,[72] which allows single-junction solar cells to maximize the utilization of incident sunlight. The superior optoelectronic characteristics of $BaZrS_3$ provide an alluring incentive for these investigations. Although there are many studies showing the characteristics of Ti or Se doping in regulating the band gap values of $BaZrS_3$, there has been little discussion of how this doping affects the stability of $BaZrS_3$. The stability of compounds is a prerequisite and foundation for their practical applications. Here, we carried out a supplementary study. In $BaZrS_3$, there are two different kinds of S that are not equal, and substituting Ti or Se for S begins with the lower-energy doped compound. As can be seen from Fig. S2(a), Se doping generally reduces the band gap of $BaZrS_3$ as the Se doping content increases. The band gap of $BaZrS_3$ can be adjusted starting from 1.732 to 1.623, 1.481, 1.623, 1.483, 1.481, 1.488, 1.558, 1.438, 1.425, 1.298, 1.334 and 1.2370 eV with Se doping contents of 0, 1/12, 2/12, 3/12, 4/12, 5/12, 6/12, 7/12, 8/12, 9/12, 10/12, 11/12 and 12/12. It should be noted, nonetheless, that Se doping has a very low modulating effect on the band gap value of $BaZrS_3$. Fig. S2(b) shows the band gap and energy above hull (e_above_hull, eV/per atom) of $BaZrS_3$ with varying Ti doping. It has been indicated that the modulation efficiency of Ti doping on the band gap value of $BaZrS_3$ is much higher that of Se,[31] which may be due to the larger differences in atomic radius between S and Ti than between S and Se. The band gap of $BaZrS_3$ can be adjusted starting from 1.732 to 1.580, 1.505, 1.316, 1.025 and 0.171 eV with Ti doping contents of 0, 1/16, 2/16, 4/16, 8/16 and 16/16. If the Ti doping content is 4/16, or 25%, the band gap of $BaZrS_3$ can be tuned to 1.316 eV. Additionally, the band gap of $BaZrS_3$ can decrease from 0.152 eV to 1.580 eV with only 6.25% Ti doping content, in line with the previously published calculation results.[73] Therefore, for the band gap modulation of $BaZrS_3$, Ti doping can be an effective method, as confirmed by published experimental data.[74] Next, using the e_above_hull criterion for the doped compounds, the impact of Ti doping on the stability of $BaZrS_3$ is investigated. The e_above_hull of the compounds changes from -0.0162 to 0.0053, -0.0015, 0.0283, 0.0655 and 0.0534 eV/per atom with Ti doping contents of 0, 1/16, 2/16, 4/16, 8/16 and 16/16. The stability of Ti-doped $BaZrS_3$ is not as good, because the majority of the e_above_hulls of the doped compounds are positive, even if their e_above_hulls are not very high and all of them are below 7 meV/per atom.[74,75] Therefore, experimental synthesis of these doped compounds with high stability could be challenging, as has been mentioned in published work.[22,74] Nevertheless, the prototypical $BaZrS_3$ with e_above_hull of -1.62 meV and good characteristics is worth further comprehensive investigation.

3.3 Intrinsic defects in BaZrS$_3$

In a ternary $BaZrS_3$ compound, the sulfur chemical potential has a significant impact on the stability and properties of the compound.[34,52,76] Furthermore, the chemical potential of sulfur (or experimental conditions) has a direct correlation with the defect features of $BaZrS_3$. This study conducts calculations for the stable chemical potential region of $BaZrS_3$ within the boundary points p1–p4 (calculation in the sequence p2–p3–p4–p1, 300 data calculation points between each boundary position). In order to provide more effective references for the experiment, the calculation results are analyzed in terms of the chemical potentials in the sequence p2–p3–p4–p1 for the chemical potential transition of S from poor to rich, as illustrated in Fig. 2. It is observed that, during this transition, the chemical potential of Ba and Zr generally decreases inside the compound stable region of $BaZrS_3$. The differential change trend between the chemical potential of the constituent elements S, Ba and Zr could have a significant impact on the

Table 1 The chemical potential boundary points p1–p4 that correspond to Fig. 1

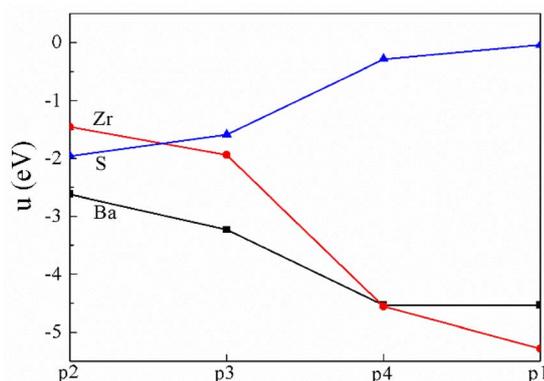| Position	Ba/eV	Zr/eV	S eV^{-1}
p2	-2.6228	-1.4553	-1.9585
p3	-3.2318	-1.9425	-1.5931
p4	-4.5381	-4.5551	-0.2868
p1	-4.5381	-5.2859	-0.0432

Fig. 2 The calculation results are analyzed in terms of the chemical potentials in the sequence of p2–p3–p4–p1, for the transition of S from poor to rich.

defect characteristics of BaZrS$_3$, which should be noted in the study.

Fig. S3 shows the formation energy of the intrinsic defects as a function of the Fermi energy (E_F, also Fermi level) in the sequence p2–p3–p4–p1 (where defects related to nonequivalent S are denoted by subscripts 1 and 2, respectively). At the starting point of p2, S is poor, but Zr is rich. Zr$_i$ is the most likely defect to form in this situation if it is evaluated solely in terms of chemical trends. The second potential defect is V$_S$ when E_F is on the conduction band minimum (CBM) side. When switching to p3, with S becoming somewhat richer, the defect characteristics of the BaZrS$_3$ compound did not show any significant alteration. Arriving at p4, S is rich at a chemical potential of −0.2868 eV, but at the same time, the chemical potential of Zr and Ba becomes low. In this case, Zr$_i$ is still the most likely defect when E_F is on the VBM side. However, V$_S$ is non-ignorable, which may be attributed to the volatile nature of S (no matter whether it is rich or not, as shown over the whole stable chemical potential region in Fig. S3). It is worth noting that V$_{Zr}$ could become dominant when E_F is on the CBM side. Finally, at p1, S becomes richest at a chemical potential of −0.0432 eV with Zr becoming poorer (Ba is kept at the same chemical potential as that of p4). The defect characteristics of the BaZrS$_3$ compound do not change significantly, except that V$_{Zr}$ becomes the most popular defect when E_F is at the CBM side. It should be noted that Zr$_i$ and V$_S$ would contribute electron carriers, but V$_{Zr}$ might serve as a carrier RC in the n-type BaZrS$_3$ compound, depending on where it is in the band.[31,77] These findings show that the defect features of BaZrS$_3$ are strongly influenced by the chemical potentials of the composition elements.

3.4 The photoelectric properties of BaZrS$_3$

The concentration of a defect α with charge state q, under thermodynamic equilibrium, is determined by its formation energy,[63,78] as indicated in eqn (f):

$$n(\alpha, q) = N_{sites}g_q e^{(-\Delta E_f/k_B T)} \tag{f}$$

where N_{sites} is the concentration of possible defect sites, g_q is the charge-dependent degeneracy factor, and ΔE_f is the defect formation energy, which can be determined from the given Fermi energy and elemental chemical potentials, as can be seen in Fig. S3.

In non-ionic materials, carriers are produced by all the ionized defects with charge state $q \neq 0$. The electron carriers are produced by positively charged donor defects with $q > 0$, and their summed charge is $\sum_{a;q>0}[q \times n(\alpha, q)]$. Conversely, the hole carriers are produced by negatively charged acceptor defects with $q < 0$, and their summed charge is $\sum_{a;q<0}[(-q) \times n(\alpha, q)]$. Both the thermal excitation and the ionization of all these defects (dopants) contribute to the final concentrations of electron and hole carriers. The equilibrium-state Fermi energy can be calculated by solving for the charge neutrality using eqn (g):

$$n_0 + \sum_{a;q<0}[(-q) \times n(a, q)] = p_0 + \sum_{a;q>0}[q \times n(a, q)] \tag{g}$$

Here, n_0 and p_0 are free carrier concentrations, which can be defined using eqn (h) and (i):

$$n_0 = \int_{\varepsilon CBM}^{+\infty} g_C(E)f(e)dE \tag{h}$$

$$p_0 = \int_{-\infty}^{\varepsilon VBM} g_V(E)(1 - f(e))dE \tag{i}$$

where $g_C(E)$ and $g_V(E)$ are the density of states for the conduction and valence bands, respectively, and $f(e)$ is the Fermi–Dirac occupation function. Both $g_C(E)$ and $g_V(E)$ can be calculated from the parabolic band approximation, as mentioned in ref. 78. Semiconductors are usually grown at high temperature and then put through a rapid annealing process to a lower working (measuring) temperature. Therefore, defects are usually formed at high temperature and then the densities of different charge states will be redistributed during the rapid annealing. Our calculation method is in accordance with such a fabrication process.[78–80] First, eqn (g) is solved at a high growth temperature (it is set at 1000 K in this study), and then the Fermi level and the densities of each defect in different charge states q can be obtained at this high temperature. Afterwards, eqn (7) is solved again at the lower measuring temperature (it is set at 300 K in this study), but now the densities of defects in different charge states do not follow eqn (f). In the second step, the density summation for each defect over all charge states is fixed at the value calculated in the first step, and the density of each charge state will undergo a redistribution according to the Fermi–Dirac occupation. Then, a new Fermi level can be obtained at the working (measuring) temperature, and the redistributed defect densities and carrier densities can be calculated.

After the defect formation energy ΔE_f has been obtained, the carrier concentration can be computed using the above-described theory, and the result is displayed in Fig. 3(a). As S gradually changes from poor to rich, for the chemical potential transformation sequence p2–p3–p4–p1, the carrier characteristics also change. Yet BaZrS$_3$ always remains n-type over the
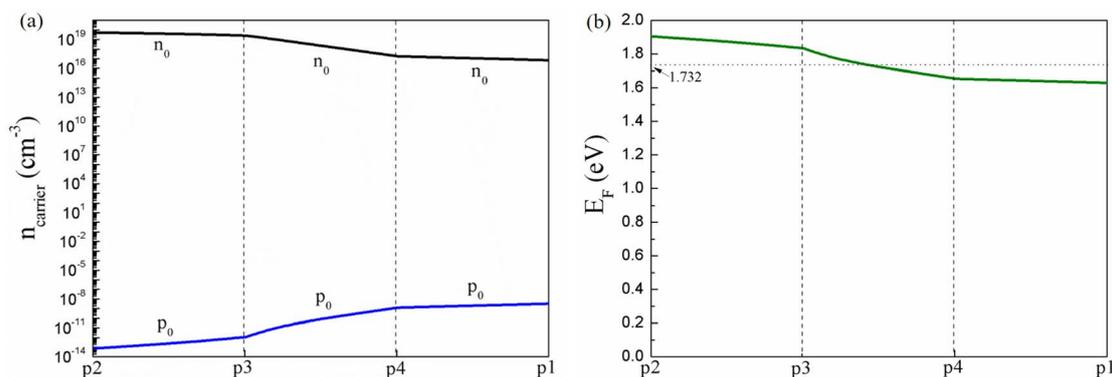
Fig. 3 The calculated carrier concentrations (a) and Fermi energy level (b) of BaZrS$_3$ in the sequence p2–p3–p4–p1.

whole stable chemical potential region, which could be due to the donor defects of V_S and Zr_i, as shown in Fig. S3. At p2, the n_0 and p_0 of BaZrS$_3$ are at 5.422919×10^{19} and 7.453176×10^{-14} cm^{-3}, respectively. At p1, the n_0 of BaZrS$_3$ decreases to 6.966194×10^{16} cm^{-3}, while p_0 rises comparatively to 3.279799×10^{-9} cm^{-3}, even though it is still much lower than n_0. The increased p_0 may come from the acceptor V_{Zr}. The properties of the carrier concentration align with the experimental findings.[23] The E_F of BaZrS$_3$ was also calculated and is displayed in Fig. 3(b), which demonstrates the changes in the semiconductor type more clearly. It is evident that BaZrS$_3$ is an n-type semiconductor over the whole stable chemical potential region. At p2 and p3, E_F is located above the CBM, indicating degenerated semiconductor formation, which might not be suitable for use in solar cells. At p4 and p1, E_F is below the CBM but close to it, which is beneficial for the generation of electron carriers. The n-type chalcogenide perovskite BaZrS$_3$ with a high intrinsic carrier concentration could have great advantages for application in semiconductors and electronics.

The transition levels of the intrinsic defects in BaZrS$_3$ were also extracted from Fig. 3S (where the defect charge state determines the slope of the line, and the turning points represent the transition energy levels between different charge states for a given defect), as shown in Fig. 4. Compared to earlier references, the results based on a large supercell of 240 atoms with an HSE06 hybrid functional and finite-size effect

correction directly display a considerably clearer band gap.[22,29] According to the published work, even when deep-level defects like V_{Zr} and S_{Zr} are present, their formation of S clusters (dimer, trimer and tetramer) tends to remove mid-gap states in the neutral charge state and leaves behind a relatively clean band gap.[29] Therefore, some deep-level defects mentioned in the published work might not actually exist in BaZrS$_3$ in its thermodynamically stable region. As displayed in Fig. 4, from the standpoint of carrier features and the degree of impact of the defects, the decisive defects are expected to be V_S, Zr_i, V_{Zr}, S_i and S_{Ba} in BaZrS$_3$. As can be seen in the figure, V_S and Zr_i are donor defects, and all of the defects are located on the CBM side. Defect S_i (+1/0) does not exist. Meanwhile, S_i (2+/0) is a donor defect and is located around the middle of the band at 0.77016 eV above the VBM, which is considered a deep-level defect. S_{Ba} (1+/0), located at 0.23845 eV above the VBM, is also a donor defect and might behave as a deep-level defect in BaZrS$_3$. From Fig. 3(a) and 4, the donor defects V_S and Zr_i could be the main contributors to n-type BaZrS$_3$, and the acceptor defect V_{Zr} could be the main contributor to the p_0 of BaZrS$_3$, even if it is quite low. Deep-level defects may act as carrier RCs, and they may have a significant impact on the performance of the fabricated device. The concentrations of deep-level defects in BaZrS$_3$ are illustrated in Fig. 5. The concentrations of defects $S_i{}^0$ and $S_{Ba}{}^0$ are high, whereas those of $S_i{}^{2+}$ and $S_{Ba}{}^{1+}$ are low, which is consistent with the results shown in Fig. S3 when E_F is
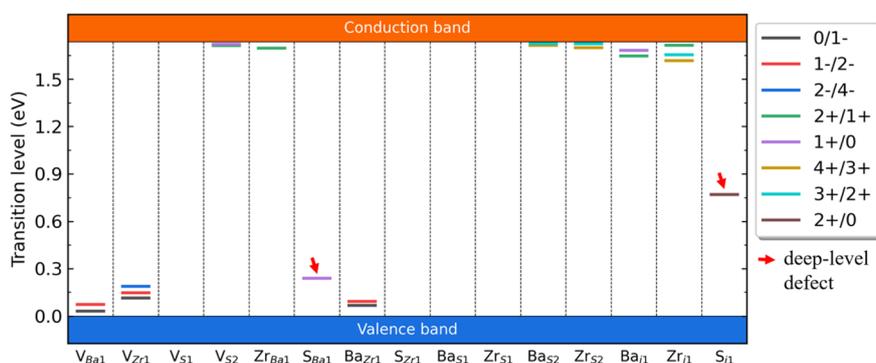

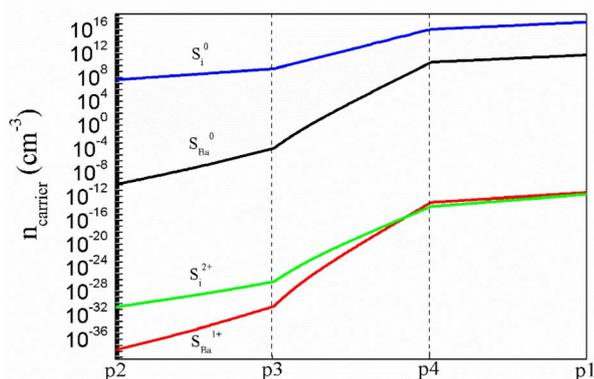Fig. 4 The transition levels of intrinsic defects (deep-level defects are also indicated by the red arrows) in BaZrS$_3$.

Fig. 5 The concentrations of deep-level defects inside the band gap of BaZrS$_3$ in the sequence p2–p3–p4–p1.

at the CBM side. The concentrations of defects S$_i^0$ and S$_{Ba}^0$ at p1 are 2.09804×10^{17} and 6.16878×10^{11} cm^{-3}, respectively. Given the extremely high concentration of deep-level defect S$_i^0$, knowledge of the carrier recombination properties of the defect is essential.

The non-radiative recombination characteristic of the deep-level defect S$_i$ with high concentration was then investigated. The carrier capture coefficients for each process were calculated in order to accurately evaluate the effect of carrier recombination characteristics of n-type BaZrS$_3$. However, it is vital to understand the recombination cycle in this instance prior to the quantitative evaluation. In n-type BaZrS$_3$, the Fermi level approaches the CBM, causing a high concentration of S$_i^0$ but a relatively low concentration of S$_i^{2+}$, which can be analyzed from the formation energy diagram in Fig. S3 and the concentrations of deep-level defects inside the band gap of BaZrS$_3$ in Fig. 5. As a result, the recombination process normally starts from S$_i^0$, first capturing two holes (it should be an excess carrier under steady-state illumination) from the VBM, becoming 2+ charged. S$_i^{2+}$ would then absorb two electrons from the CBM to return to neutral. One rate-limiting step is the minority (hole)

carrier capture by S$_i^0$. Thus, the overall recombination rate will be determined by hole capture between the neutral (q0) and 2+ charge (q2) states. Therefore, for the BaZrS$_3$ system, the donor defect S$_i$ (2+/0) with capture of minority carrier holes from the neutral (q0) to the 2+ charge (q2) state was studied extensively. The results are shown in Fig. 6.[66] We first calculated the configuration coordinate (CC) diagram for the 0/2+ transition of S$_i^0$, as shown in Fig. 6(a), where the red curve is the ground-state potential energy surface (PES) of S$_i^0$, and the blue curve is its excited-state PES. The CC diagram in Fig. 6(a) demonstrates the configuration-dependent features of the non-radiative recombination dynamics of defect S$_i$. According to the calculation, the ΔQ between two structures is 10.3942 amu$^{1/2}$ Å. The barrier for the non-radiative process shifted upward according to the neutral (q0) and 2+ charge (q2) state transition level is 1.04037 eV, which is reasonable for the transition level value of 0.77 eV (as mentioned above for Fig. 4) of S$_i$ (2+/0). Using a configuration coordinate diagram, according to the theory and method described in ref. 66 and 67, the W_{if} and other parameters in eqn (c) can be calculated and the temperature-dependent capture coefficient for minority (hole) carrier could be obtained, as shown in Fig. 6(b). It can be observed from the results that the carrier capture coefficient for minority (hole) carrier at 300.0 K is 1.28682×10^{-25} cm^3 s^{-1}, which is extremely small. It can be predicted that the electron capture coefficient should likewise be minimal. The calculated result shows that the carrier capture coefficient for the majority (electron) carrier at 300.0 K is 4.37809×10^{-23} cm^3 s^{-1}, as the concentration of electron carriers at p1 is very high at 6.966194×10^{16} cm^{-3}, much higher than that of holes with a concentration of 3.279799×10^{-9} cm^{-3}. Therefore, for the deep-level defect of S$_i$, the carrier recombination characteristics are still decided by the minority carrier hole, which shows an extremely low non-radiative carrier capture coefficient. The carrier capture coefficient of another deep-level defect, S$_{Ba}$, at 300.0 K was also calculated, and it is also very low at 1.52933×10^{-20} cm^3 s^{-1}. Therefore, the chalcogenide perovskite BaZrS$_3$ could in fact be
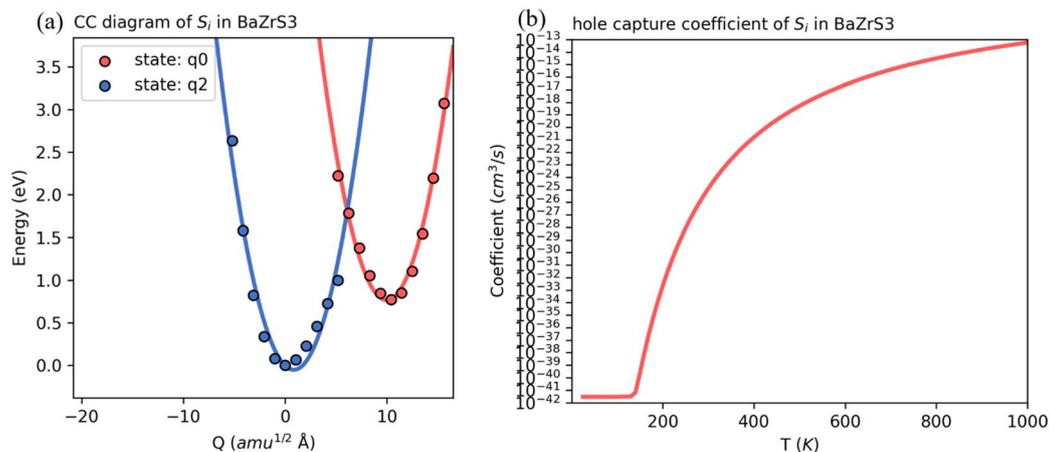

Fig. 6 (a) The configuration coordinate (CC) diagram for non-radiative calculation (b) and corresponding temperature-dependent hole capture coefficient of S$_i$ from q0 to q2 in BaZrS$_3$.
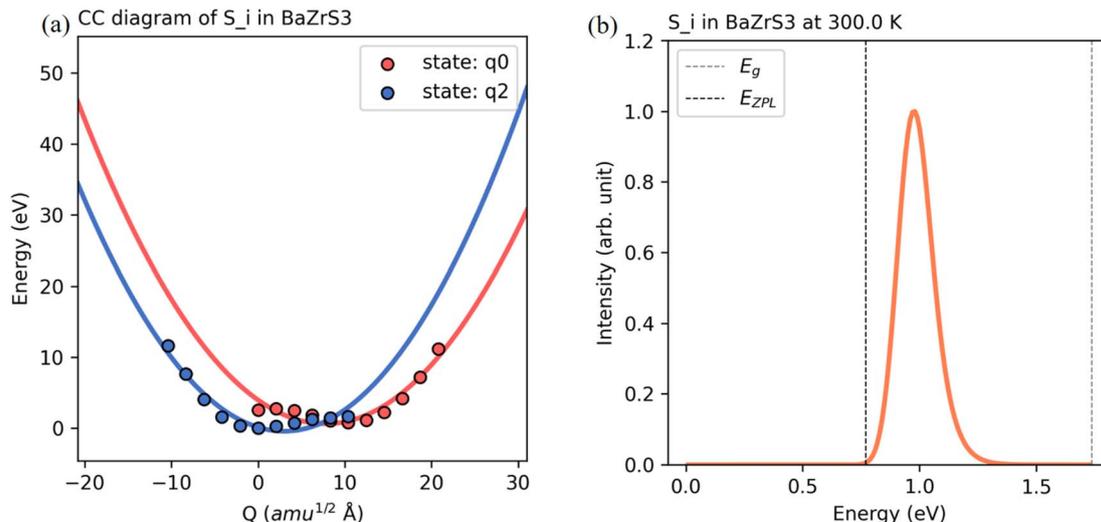
Fig. 7 (a) The configuration coordinate (CC) diagram for radiative calculation (b) and corresponding PL lineshape spectrum of S_i from q0 to q2 in BaZrS$_3$.

defect tolerant,[43,48,49,81–83] which is of crucial importance for its further development and application in photoelectric devices.

Fig. 7 displays the results of an investigation into the radiative recombination characteristic of the deep-level donor defect of S_i (2+/0). The radiative recombination process shows clear configuration–lattice coupling features, as can be seen from the CC diagram in Fig. 7(a). The ΔQ between two structures is also the same at 10.3942 amu$^{1/2}$ Å. According to the calculations, the lattice relaxation energy is 1.5691 eV. The emission energy is 0.7991 eV. Therefore, the result is consistent with the transition level value 0.77 eV of S_i (2+/0). The PL spectrum in Fig. 7(b) indicates that the position of the peak in the lineshape is 0.98 eV. Compared to the transition level value 0.77 eV of S_i (2+/0), it is slightly larger but reasonable for radiative recombination of this defect. The full width at half maxima of the lineshape is 0.16 eV. The volume of this supercell was assessed at around 6.08×10^{-21} cm^{-3}. Therefore, the radiative carrier capture coefficient was calculated to be 3.51×10^{-15} cm^3 s^{-1}, which is also quite good.[82]

Using a solar cell capacitor simulator from the University of Gent in Belgium, the photoelectric conversion properties of BaZrS$_3$ were computed by employing Poisson's equation and continuity equations for electron and hole carriers.[84] [C$_6$H$_4$-N(C$_6$H$_2$(CH$_3$)$_3$)C$_6$H$_4$]$_n$ (PTAA) shows good transparency for visible light, mechanical flexibility, conductivity and stability. Additionally, it has received certification for highly effective perovskite solar cells. In this study, the effects of the carrier and defect characteristics on the performance of the strong n-type BaZrS$_3$ were simulated, based on a BaZrS$_3$-PTAA single-junction solar cell without an electron transport layer (ETL), which is of great significance to the simple and controllable preparation of BaZrS$_3$ solar cells. First, the p1 point with rich S was studied. The thin-film thickness of PTAA was set at 10 nm, and other essential input parameters were obtained from the above calculations and published ref. 85 and 86. To examine the

effect of the thickness of BaZrS$_3$, the thin-film thickness of BaZrS$_3$ was varied from 100 to 1000 nm in steps of 100 nm, while the other parameters were fixed. It was found that BaZrS$_3$, with its previously mentioned superior light absorption, might absorb most of the incident sunlight (standard AM1.5) with a thickness of less than 100 nm. Thus, in order to find the optimal value, the BaZrS$_3$ thin-film thickness was further varied from 10 to 100 nm in steps of 10 nm. This revealed that, BaZrS$_3$ with a thickness of only 80 nm, can absorb the majority of incident sunlight with a conversion efficiency of 22.04%, as shown in Fig. S4(a).

The photoelectric performances of BaZrS$_3$ at stable chemical potential points p2, p3 and p4 were also studied (solar cell parameters were all set the same, but without those related to chemical potential), and the results are displayed in Fig. S4(b) and Table S1, together with that of p1. As can be seen from the results, p2 and p3 with very high n_0 (see Fig. 3), which lead E_F into the CBM, turn out to show low conversion efficiency, which could be due to the degenerated semiconductor characteristics. Arriving at p4 with n_0 falling and E_F sliding to below the CBM, the conversion efficiency of BaZrS$_3$ quickly rises to 21.96%. At p1, the conversion efficiency of BaZrS$_3$ becomes 22.04%. The high conversion efficiency of BaZrS$_3$ could be attributed to the high n_0 and excellent defect tolerance, which indicates that BaZrS$_3$ is an excellent photovoltaic material. Moreover, the conversion efficiency of BaZrS$_3$ could readily approach 25.46%, as shown by p1$^+$ in Fig. S4(b) and Table S1, when the ΔVBM between BaZrS$_3$ and PTAA was decreased to 0.1 eV by modifying the VBM value of PTAA, as this can further improve the V_{oc} of the BaZrS$_3$ solar cell from 1.23 to 1.45 eV. All these results demonstrate the superior photovoltaic capabilities of BaZrS$_3$.

4 Conclusion

The defect and carrier characteristics of BaZrS$_3$ were studied by first-principles calculations using a 240-atom supercell with

HSE06 hybrid functional and finite-size effect correction. The stable chemical potential range was determined, where $BaZrS_3$ is thermodynamically stable against the formation of its three constituent elements and four competitive secondary phase compounds (i.e., $Ba_3Zr_2S_7$, Zr_3S_4, ZrS_3 and ZrS_2). This indicated that $BaZrS_3$ with e_above_hull of −1.62 meV has good thermodynamic stability. The chemical potential boundary points were indicated as p1 (μ_{Ba} −4.5381, μ_{Zr} −5.2859 and μ_S −0.0432 eV), p2 (μ_{Ba} −2.6228, μ_{Zr} −1.4553 and μ_S −1.9585 eV), p3 (μ_{Ba} −3.2318, μ_{Zr} −1.9425 and μ_S −1.5931 eV) and p4 (μ_{Ba} −4.5381, μ_{Zr} −4.5551 and μ_S 0.2868 eV). The formation energy of intrinsic defects in $BaZrS_3$ was studied according to the chemical potential transition of S from poor to rich in the sequence p2–p3–p4–p1. As the chemical potential of S increases in the sequence p2–p3–p4–p1, the carrier characteristics in $BaZrS_3$ also change. Yet $BaZrS_3$ always remains n-type over the whole stable chemical potential region, which could be due to the donor defects of V_S and Zr_i. At p2, the n_0 and p_0 of $BaZrS_3$ are 5.422919×10^{19} and 7.453176×10^{-14} cm^{-3}, respectively. At p1, the n_0 of $BaZrS_3$ decreases to 6.966194×10^{16} cm^{-3}, while p_0 rises comparatively to 3.279799×10^9 cm^{-3}, even though it is still much lower than n_0. The increased p0 may come from the acceptor V_{Zr}. The properties of the carrier concentration align with the experimental findings. The transition levels of the intrinsic defects in $BaZrS_3$ show a much cleaner band gap than that in previously reported references. S_i (2+/0) and S_{Ba} (1+/0) are shown to be deep-level donors, located around the middle of the band at 0.77016 eV and 0.23845 eV above the VBM, respectively. The donor defects V_S and Zr_i could be the main contributors to n-type $BaZrS_3$, while the deep-level defects may behave as carrier recombination centers in $BaZrS_3$. The concentrations of defects S_i^0 and S_{Ba}^0 at p1 are 2.09804×10^{17} and 6.16878×10^{11} cm^{-3}, respectively. The concentration of deep-level defect S_i^0 is very high, and the carrier recombination characteristics of the defect were thus further studied. However, the results show that its non-radiative capture coefficient for the minority (hole) carrier at 300.0 K is extremely small, at 1.28682×10^{-25} cm^3 s^{-1}. Its radiative capture coefficient is also likewise quite good at 3.51×10^{-15} cm^3 s^{-1}, indicating its defect tolerance characteristics.

Based on the carrier and defect characteristics, the photoelectric properties of $BaZrS_3$ were further examined with PTAA as its partner hole transport layer, excluding the electron transport layer. This indicated that p2 and p3, with very high n_0 that leads E_F into the CBM, turn out to show low conversion efficiency, which could be due to the degenerate semiconductor characteristics. At p1, the results show that $BaZrS_3$ with just 80 nm can absorb most of the incident sunlight and shows a conversion efficiency of 22.04%, which is sufficient for commercial use. The high conversion efficiency of $BaZrS_3$ could be attributed to the high n_0 and excellent defect tolerance. Moreover, the conversion efficiency of $BaZrS_3$ could approach 25.46% when the ΔVBM between $BaZrS_3$ and PTAA is lowered to 0.1 eV, demonstrating the exceptional photovoltaic capabilities of $BaZrS_3$.

This work has elucidated the influence of defects and carriers on the photoelectric properties of $BaZrS_3$, which can help clarify the true upper limit of conversion efficiency and aid in the experimental, controllable preparation of high-quality $BaZrS_3$ films and devices. This work might also open a path to a direct connection between practical synthesis protocols and crystal defect features, which is of crucial importance for the further development and application of relevant photoelectric devices.

Author contributions

Qinmiao Chen: funding acquisition, conceptualization, investigation, writing – original draft. Yi Ni: investigation, formal analysis. Yufei Wang: methodology, investigation, writing – review & editing.

Conflicts of interest

There are no conflicts of interest to declare.

Data availability

The data supporting this article have been included as part of the manuscript and supplementary information (SI). Other datasets that may support the current study are available from the corresponding author on reasonable request. Supplementary information: optical characteristics of $BaZrS_3$; influence of element doping on the band and thermodynamically stability of $BaZrS_3$; formation energy of intrinsic defects in $BaZrS_3$ as a function of the Fermi energy; photoelectric conversion characteristics of the modeled $BaZrS_3$ solar cell. See DOI: https://doi.org/10.1039/d5ra07387a.

Acknowledgements

References

1 J. Burschka, N. Pellet, S. J. Moon, R. Humphry-Baker, P. Gao, M. K. Nazeeruddin and M. Gratzel, Sequential deposition as a route to high-performance perovskite-sensitized solar cells, Nature, 2013, 499(7458), 316–319.

2 G. Xing, N. Mathews, S. Sun, S. S. Lim, Y. M. Lam, M. Grätzel, S. Mhaisalkar and T. C. Sum, Long-Range Balanced Electron- and Hole-Transport Lengths in Organic-Inorganic $CH_3NH_3PbI_3$, Science, 2013, 342(6156), 344–347.

3 S. D. Stranks, G. E. Eperon, G. Grancini, C. Menelaou, M. J. P. Alcocer, T. Leijtens, L. M. Herz, A. Petrozza and H. J. Snaith, Electron-Hole Diffusion Lengths Exceeding 1 Micrometer in an Organometal Trihalide Perovskite Absorber, Science, 2013, 342(6156), 341–344.

4 H. P. Zhou, Q. Chen, G. Li, S. Luo, T. B. Song, H. S. Duan, Z. R. Hong, J. B. You, Y. S. Liu and Y. Yang, Interface engineering of highly efficient perovskite solar cells, Science, 2014, 345(6196), 542–546.

5 Y. X. Gao, Y. N. Dong, K. Q. Huang, C. J. Zhang, B. Liu, S. T. Wang, J. Shi, H. P. Xie, H. Huang, S. Xiao, J. He,

Y. L. Gao, R. A. Hatton and J. L. Yang, Highly Efficient, Solution-Processed CsPbl(2)Br Planar Heterojunction Perovskite Solar Cells via Flash Annealing, *ACS Photonics*, 2018, **5**(10), 4104–4110.

6 L. T. Dou, Y. Yang, J. B. You, Z. R. Hong, W. H. Chang, G. Li and Y. Yang, Solution-processed hybrid perovskite photodetectors with high detectivity, *Nat. Commun.*, 2014, **5**, 5404.

7 P. Büchele, M. Richter, S. F. Tedde, G. J. Matt, G. N. Ankah, R. Fischer, M. Biele, W. Metzger, S. Lilliu, O. Bikondoa, J. E. Macdonald, C. J. Brabec, T. Kraus, U. Lemmer and O. Schmidt, X-ray imaging with scintillator-sensitized hybrid organic photodetectors, *Nat. Photonics*, 2015, **9**(12), 843–848.

8 B. R. Sutherland, A. K. Johnston, A. H. Ip, J. X. Xu, V. Adinolfi, P. Kanjanaboos and E. H. Sargent, Sensitive, Fast, and Stable Perovskite Photodetectors Exploiting Interface Engineering, *ACS Photonics*, 2015, **2**(8), 1117–1123.

9 L. Q. Zhang, X. L. Yang, Q. Jiang, P. Y. Wang, Z. G. Yin, X. W. Zhang, H. R. Tan, Y. Yang, M. Y. Wei, B. R. Sutherland, E. H. Sargent and J. B. You, Ultra-bright and highly efficient inorganic based perovskite light-emitting diodes, *Nat. Commun.*, 2017, **8**, 15640.

10 K. B. Lin, J. Xing, L. N. Quan, F. P. G. de Arquer, X. W. Gong, J. X. Lu, L. Q. Xie, W. J. Zhao, D. Zhang, C. Z. Yan, W. Q. Li, X. Y. Liu, Y. Lu, J. Kirman, E. H. Sargent, Q. H. Xiong and Z. H. Wei, Perovskite light-emitting diodes with external quantum efficiency exceeding 20 percent, *Nature*, 2018, **562**(7726), 245–248.

11 L. Gao, L. N. Quan, F. P. G. de Arquer, Y. B. Zhao, R. Munir, A. Proppe, R. Quintero-Bermudez, C. Q. Zou, Z. Y. Yang, M. I. Saidaminov, O. Voznyy, S. Kinge, Z. H. Lu, S. O. Kelley, A. Amassian, J. Tang and E. H. Sargent, Efficient near-infrared light-emitting diodes based on quantum dots in layered perovskite, *Nat. Photonics*, 2020, **14**(4), 227–233.

12 A. Amat, E. Mosconi, E. Ronca, C. Quarti, P. Umari, M. K. Nazeeruddin, M. Grätzel and F. De Angelis, Cation-Induced Band-Gap Tuning in Organohalide Perovskites: Interplay of Spin–Orbit Coupling and Octahedra Tilting, *Nano Lett.*, 2014, **14**(6), 3608–3616.

13 R. Prasanna, A. Gold-Parker, T. Leijtens, B. Conings, A. Babayigit, H.-G. Boyen, M. F. Toney and M. D. McGehee, Band Gap Tuning via Lattice Contraction and Octahedral Tilting in Perovskite Materials for Photovoltaics, *J. Am. Chem. Soc.*, 2017, **139**(32), 11117–11124.

14 Y. G. Rong, Y. Hu, A. Y. Mei, H. R. Tan, M. I. Saidaminov, S. I. Seok, M. D. McGehee, E. H. Sargent and H. W. Han, Challenges for commercializing perovskite solar cells, *Science*, 2018, **361**(6408), eaat8235.

15 J. P. Correa-Baena, M. Saliba, T. Buonassisi, M. Gratzel, A. Abate, W. Tress and A. Hagfeldt, Promises and challenges of perovskite solar cells, *Science*, 2017, **358**(6364), 739–744.

16 M. Gratzel, The light and shade of perovskite solar cells, *Nat. Mater.*, 2014, **13**(9), 838–842.

17 M. D. McGehee, Fast-track solar cells, *Nature*, 2013, **501**(7467), 323–325.

18 H. Hahn and U. Mutschke, Untersuchungen über ternäre Chalkogenide. XI. Versuche zur Darstellung von Thioperowskiten, *Z. Anorg. Allg. Chem.*, 1957, **288**(5–6), 269–278.

19 M. Ishii, M. Saeki and M. Sekita, Vibrational spectra of barium-zirconium sulfides, *Mater. Res. Bull.*, 1993, **28**(5), 493–500.

20 J. W. Bennett, I. Grinberg and A. M. Rappe, Effect of substituting of S for O: The sulfide perovskite BaZrS3 investigated with density, *Phys. Rev. B: Condens. Matter Mater. Phys.*, 2009, **79**(23), 235115.

21 J. A. Brehm, J. W. Bennett, M. R. Schoenberg, I. Grinberg and A. M. Rappe, The structural diversity of ABS3 compounds with d(0) electronic configuration for the B-cation, *J. Chem. Phys.*, 2014, **140**(22), 224703.

22 W. Meng, B. Saparov, F. Hong, J. Wang, D. B. Mitzi and Y. Yan, Alloying and Defect Control within Chalcogenide Perovskites for Optimized Photovoltaic Application, *Chem. Mater.*, 2016, **28**(3), 821–829.

23 X. Wei, H. Hui, C. Zhao, C. Deng, M. Han, Z. Yu, A. Sheng, P. Roy, A. Chen, J. Lin, D. F. Watson, Y.-Y. Sun, T. Thomay, S. Yang, Q. Jia, S. Zhang and H. Zeng, Realization of BaZrS3 chalcogenide perovskite thin films for optoelectronics, *Nano Energy*, 2020, **68**, 104317.

24 Z. Yu, X. Wei, Y. Zheng, H. Hui, M. Bian, S. Dhole, J.-H. Seo, Y.-Y. Sun, Q. Jia, S. Zhang, S. Yang and H. Zeng, Chalcogenide perovskite BaZrS3 thin-film electronic and optoelectronic devices by low temperature processing, *Nano Energy*, 2021, **85**, 105959.

25 M. G. Ju, J. Dai, L. Ma and X. C. Zeng, Perovskite Chalcogenides with Optimal Bandgap and Desired Optical Absorption for Photovoltaic Devices, *Adv. Energy Mater.*, 2017, **7**(18), 1700216.

26 A. Swarnkar, W. J. Mir, R. Chakraborty, M. Jagadeeswararao, T. Sheikh and A. Nag, Are Chalcogenide Perovskites an Emerging Class of Semiconductors for Optoelectronic Properties and Solar Cell?, *Chem. Mater.*, 2019, **31**(3), 565–575.

27 Y.-Y. Sun, M. L. Agiorgousis, P. Zhang and S. Zhang, Chalcogenide Perovskites for Photovoltaics, *Nano Lett.*, 2015, **15**(1), 581–585.

28 I. Sadeghi, K. Ye, M. Xu, Y. Li, J. M. LeBeau and R. Jaramillo, Making BaZrS3 Chalcogenide Perovskite Thin Films by Molecular Beam Epitaxy, *Adv. Funct. Mater.*, 2021, **31**(45), 2105563.

29 X. Wu, W. Gao, J. Chai, C. Ming, M. Chen, H. Zeng, P. Zhang, S. Zhang and Y.-Y. Sun, Defect tolerance in chalcogenide perovskite photovoltaic material BaZrS3, *Sci. China Mater.*, 2021, **64**(12), 2976–2986.

30 R. Yang, A. D. Jess, C. Fai and C. J. Hages, Low-Temperature, Solution-Based Synthesis of Luminescent Chalcogenide Perovskite BaZrS3 Nanoparticles, *J. Am. Chem. Soc.*, 2022, **144**(35), 15928–15931.

31 Y. Han, J. Xu, Y. Liang, X. Chen, M. Jia, J. Zhang, L. Lian, Y. Liu, X. Li and Z. Shi, P-type conductive BaZrS3 thin film

and its band gap tunning via Ruddlesden-Popper Ba3Zr2S7 and titanium alloying, *Chem. Eng. J.*, 2023, **473**, 145351.

32 A. A. Pradhan, M. C. Uible, S. Agarwal, J. W. Turnley, S. Khandelwal, J. M. Peterson, D. D. Blach, R. N. Swope, L. Huang, S. C. Bart and R. Agrawal, Synthesis of BaZrS3 and BaHfS3 Chalcogenide Perovskite Films Using Single-Phase Molecular Precursors at Moderate Temperatures, *Angew. Chem., Int. Ed.*, 2023, **62**(15), e202301049.

33 S. Riva, S. Mukherjee, S. M. Butorin, C. Comparotto, G. Aggarwal, E. Johannesson, M. Abdel-Hafiez, J. Scragg and H. Rensmo, Electronic Structure and Surface Chemistry of BaZrS3 Perovskite Powder and Sputtered Thin Film, *ACS Appl. Mater. Interfaces*, 2024, **16**(30), 40210–40221.

34 B. Zhao, H. Chen, R. Ahsan, F. Hou, E. R. Hoglund, S. Singh, M. Shanmugasundaram, H. Zhao, A. V. Krayev, H. Htoon, P. E. Hopkins, J. Seidel, R. Kapadia and J. Ravichandran, Photoconductive Effects in Single Crystals of BaZrS3, *ACS Photonics*, 2024, **11**(3), 1109–1116.

35 R. Lelieveld and D. J. W. IJdo, Sulphides with the GdFeO3 structure, *Acta Crystallogr., Sect. B*, 1980, **36**(10), 2223–2226.

36 C.-S. Lee, K. M. Kleinke and H. Kleinke, Synthesis, structure, and electronic and physical properties of the two SrZrS3 modifications, *Solid State Sci.*, 2005, **7**(9), 1049–1054.

37 H. Brasseur and L. Pauling, The Crystal Structure of Ammonium Cadmium Chloride, NH4CdCl3, *J. Am. Chem. Soc.*, 1938, **60**(12), 2886–2890.

38 A. Clearfield, The synthesis and crystal structures of some alkaline earth titanium and zirconium sulfides, *Acta Crystallogr.*, 1963, **16**(2), 135–142.

39 Y. Takeda, F. Kanamura, M. Shimada and M. Koizumi, The crystal structure of BaNiO3, *Acta Crystallogr., Sect. B*, 1976, **32**(8), 2464–2466.

40 P. Caprioglio, C. M. Wolff, O. J. Sandberg, A. Armin, B. Rech, S. Albrecht, D. Neher and M. Stolterfoht, On the Origin of the Ideality Factor in Perovskite Solar Cells, *Adv. Energy Mater.*, 2020, **10**(27), 2000502.

41 W. C. Xiang and W. Tress, Review on Recent Progress of All-Inorganic Metal Halide Perovskites and Solar Cells, *Adv. Mater.*, 2019, **31**(44), 1902851.

42 Z. W. Xiao and Y. F. Yan, Progress in Theoretical Study of Metal Halide Perovskite Solar Cell Materials, *Adv. Energy Mater.*, 2017, **7**(22), 1701136.

43 M. Yavari, F. Ebadi, S. Meloni, Z. S. Wang, T. C. J. Yang, S. J. Sun, H. Schwartz, Z. W. Wang, B. Niesen, J. Durantini, P. Rieder, K. Tvingstedt, T. Buonassisi, W. C. H. Choy, A. Filippetti, T. Dittrich, S. Olthof, J. P. Correa-Baena and W. Tress, How far does the defect tolerance of lead-halide perovskites range? The example of Bi impurities introducing efficient recombination centers, *J. Mater. Chem. A*, 2019, **7**(41), 23838–23853.

44 W.-J. Yin, T. Shi and Y. Yan, Unusual defect physics in CH3NH3PbI3 perovskite solar cell absorber, *Appl. Phys. Lett.*, 2014, **104**(6), 063903.

45 H. R. Tan, A. Jain, O. Voznyy, X. Z. Lan, F. P. G. de Arquer, J. Z. Fan, R. Quintero-Bermudez, M. J. Yuan, B. Zhang, Y. C. Zhao, F. J. Fan, P. C. Li, L. N. Quan, Y. B. Zhao, Z. H. Lu, Z. Y. Yang, S. Hoogland and E. H. Sargent, Efficient and stable solution-processed planar perovskite solar cells via contact passivation, *Science*, 2017, **355**(6326), 722–726.

46 J. Haruyama, K. Sodeyama, L. Y. Han and Y. Tateyama, Surface Properties of CH3NH3PbI3 for Perovskite Solar Cells, *Acc. Chem. Res.*, 2016, **49**(3), 554–561.

47 J. Kim, S.-H. Lee, J. H. Lee and K.-H. Hong, The Role of Intrinsic Defects in Methylammonium Lead Iodide Perovskite, *J. Phys. Chem. Lett.*, 2014, **5**(8), 1312–1317.

48 R. E. Brandt, J. R. Poindexter, P. Gorai, R. C. Kurchin, R. L. Z. Hoye, L. Nienhaus, M. W. B. Wilson, J. A. Polizzotti, R. Sereika, R. Žaltauskas, L. C. Lee, J. L. MacManus-Driscoll, M. Bawendi, V. Stevanović and T. Buonassisi, Searching for "Defect-Tolerant" Photovoltaic Materials: Combined Theoretical and Experimental Screening, *Chem. Mater.*, 2017, **29**(11), 4667–4674.

49 R. E. Brandt, V. Stevanović, D. S. Ginley and T. Buonassisi, Identifying defect-tolerant semiconductors with high minority-carrier lifetimes: beyond hybrid lead halide perovskites, *MRS Commun.*, 2015, **5**(2), 265–275.

50 J. S. Park, S. Kim, Z. Xie and A. Walsh, Point defect engineering in thin-film solar cells, *Nat. Rev. Mater.*, 2018, **3**(7), 194–210.

51 J. Kang and L.-W. Wang, High Defect Tolerance in Lead Halide Perovskite CsPbBr3, *J. Phys. Chem. Lett.*, 2017, **8**(2), 489–493.

52 M. Surendran, H. Chen, B. Zhao, A. S. Thind, S. Singh, T. Orvis, H. Zhao, J.-K. Han, H. Htoon, M. Kawasaki, R. Mishra and J. Ravichandran, Epitaxial Thin Films of a Chalcogenide Perovskite, *Chem. Mater.*, 2021, **33**(18), 7457–7464.

53 J. Furthmüller, J. Hafner and G. Kresse, Ab initiocalculation of the structural and electronic properties of carbon and boron nitride using ultrasoft pseudopotentials, *Phys. Rev. B: Condens. Matter Mater. Phys.*, 1994, **50**(21), 15606–15622.

54 J. P. Perdew, J. A. Chevary, S. H. Vosko, K. A. Jackson, M. R. Pederson, D. J. Singh and C. Fiolhais, Atoms, molecules, solids, and surfaces: Applications of the generalized gradient approximation for exchange and correlation, *Phys. Rev. B: Condens. Matter Mater. Phys.*, 1992, (11), 6671–6687.

55 M. L. Huang, Z. N. Zheng, Z. X. Dai, X. Guo, S. S. Wang, L. L. Jiang, J. C. Wei and S. Y. Chen, DASP: Defect and Dopant ab-initio Simulation Package, *J. Semicond.*, 2022, **43**, 82–95.

56 J. Taylor, H. Guo and J. Wang, Ab initio modeling of quantum transport properties of molecular electronic devices, *Phys. Rev. B: Condens. Matter Mater. Phys.*, 2001, **63**(24), 245407.

57 P. E. Blöchl, Projector augmented-wave method, *Phys. Rev. B: Condens. Matter Mater. Phys.*, 1994, **50**(24), 17953–17979.

58 J. Zhang, X. Chen, M. Deng, H. Shen, H. Li and J. Ding, Effects of native defects and cerium impurity on the monoclinic BiVO4 photocatalyst obtained via PBE+U calculations, *Phys. Chem. Chem. Phys.*, 2020, **22**(43), 25297–25305.

59 S. B. Zhang, S. H. Wei, A. Zunger and H. Katayama-Yoshida, Defect physics of the CuInSe 2 chalcopyrite semiconductor, *Phys. Rev. B: Condens. Matter Mater. Phys.*, 1998, **57**(16), 9642–9656.

60 J. Heyd and G. E. Scuseria, Efficient hybrid density functional calculations in solids: Assessment of the Heyd–Scuseria–Ernzerhof screened Coulomb hybrid functional, *J. Chem. Phys.*, 2004, **121**(3), 1187–1192.

61 J. Pohl and K. Albe, Intrinsic point defects in CuInSe2 and CuGaSe2 as seen via screened-exchange hybrid density functional theory, *Phys. Rev. B: Condens. Matter Mater. Phys.*, 2013, **87**(24), 3249–3253.

62 C. Freysoldt, J. Neugebauer and C. G. Van de Walle, Fully Ab Initio Finite-Size Corrections for Charged-Defect Supercell Calculations, *Phys. Rev. Lett.*, 2009, **102**(1), 016402.

63 C. Freysoldt, B. Grabowski, T. Hickel, J. Neugebauer, G. Kresse, A. Janotti and C. G. Van de Walle, First-principles calculations for point defects in solids, *Rev. Mod. Phys.*, 2014, **86**(1), 253–305.

64 D. B. Laks, C. G. Van de Walle, G. F. Neumark, P. E. Blöchl and S. T. Pantelides, Native defects and self-compensation in ZnSe, *Phys. Rev. B: Condens. Matter Mater. Phys.*, 1992, **45**(19), 10965–10978.

65 S. H. Wei, Overcoming the doping bottleneck in semiconductors, *Comput. Mater. Sci.*, 2004, **30**(3–4), 337–348.

66 A. Alkauskas, Q. Yan and C. G. Van de Walle, First-principles theory of nonradiative carrier capture via multiphonon emission, *Phys. Rev. B: Condens. Matter Mater. Phys.*, 2014, **90**(7), 075202.

67 M. E. Turiansky, A. Alkauskas, M. Engel, G. Kresse, D. Wickramaratne, J.-X. Shen, C. E. Dreyer and C. G. Van de Walle, Nonrad: Computing nonradiative capture coefficients from first principles, *Comput. Phys. Commun.*, 2021, **267**, 108056.

68 H. I. Eya and N. Y. Dzade, Density Functional Theory Insights into the Structural, Electronic, Optical, Surface, and Band Alignment Properties of BaZrS3 Chalcogenide Perovskite for Photovoltaics, *ACS Appl. Energy Mater.*, 2023, **6**(11), 5729–5738.

69 S. De Wolf, J. Holovsky, S.-J. Moon, P. Löper, B. Niesen, M. Ledinsky, F.-J. Haug, J.-H. Yum and C. Ballif, Organometallic Halide Perovskites: Sharp Optical Absorption Edge and Its Relation to Photovoltaic Performance, *J. Phys. Chem. Lett.*, 2014, **5**(6), 1035–1039.

70 W. C. Dunlap and R. L. Watters, Direct Measurement of the Dielectric Constants of Silicon and Germanium, *Phys. Rev.*, 1953, **92**(6), 1396–1397.

71 M. Hirasawa, T. Ishihara, T. Goto, K. Uchida and N. Miura, Magnetoabsorption of the lowest exciton in perovskite-type compound (CH3NH3)PbI3, *Physica B*, 1994, **201**, 427–430.

72 W. Shockley and H. J. Queisser, Detailed Balance Limit of Efficiency of p-n Junction Solar Cells, *J. Appl. Phys.*, 1961, **32**(3), 510–519.

73 M. B. Kanoun, B. Ul Haq, A.-A. Kanoun and S. Goumri-Said, Ti Alloying as a Route to BaZrS3 Chalcogenide Perovskite with Enhanced Photovoltaic Performance, *Energy Fuels*, 2023, **37**(13), 9548–9556.

74 X. Wei, H. Hui, S. Perera, A. Sheng, D. F. Watson, Y.-Y. Sun, Q. Jia, S. Zhang and H. Zeng, Ti-Alloying of BaZrS3 Chalcogenide Perovskite for Photovoltaics, *ACS Omega*, 2020, **5**(30), 18579–18583.

75 K. V. Sopiha, C. Comparotto, J. A. Márquez and J. J. S. Scragg, Chalcogenide Perovskites: Tantalizing Prospects, Challenging Materials, *Adv. Opt. Mater.*, 2021, **10**(3), 2101704.

76 R. Yang, J. Nelson, C. Fai, H. A. Yetkin, C. Werner, M. Tervil, A. D. Jess, P. J. Dale and C. J. Hages, A Low-Temperature Growth Mechanism for Chalcogenide Perovskites, *Chem. Mater.*, 2023, **35**(12), 4743–4750.

77 J. Q. Li, Z. K. Yuan, S. Y. Chen, X. G. Gong and S. H. Wei, Effective and Noneffective Recombination Center Defects in Cu2ZnSnS4: Significant Difference in Carrier Capture Cross Sections, *Chem. Mater.*, 2019, **31**(3), 826–833.

78 J. Ma, S. H. Wei, T. A. Gessert and K. K. Chin, Carrier density and compensation in semiconductors with multiple dopants and multiple transition energy levels: Case of Cu impurities in CdTe, *Phys. Rev. B: Condens. Matter Mater. Phys.*, 2011, **83**(24), 245207.

79 J. H. Yang, J. S. Park, J. Kang, W. Metzger, T. Barnes and S. H. Wei, Tuning the Fermi level beyond the equilibrium doping limit through quenching: The case of CdTe, *Phys. Rev. B: Condens. Matter Mater. Phys.*, 2014, **90**(24), 245202.

80 J. C. Wei, L. L. Jiang, M. L. Huang, Y. N. Wu and S. Y. Chen, Intrinsic Defect Limit to the Growth of Orthorhombic HfO2 and (Hf,Zr)O2 with Strong Ferroelectricity: First-Principles Insights, *Adv. Funct. Mater.*, 2021, **31**(42), 2104913.

81 K. Ye, B. Zhao, B. T. Diroll, J. Ravichandran and R. Jaramillo, Time-resolved photoluminescence studies of perovskite chalcogenides, *Faraday Discuss.*, 2022, **239**, 146–159.

82 O. E. Semonin, G. A. Elbaz, D. B. Straus, T. D. Hull, D. W. Paley, A. M. van der Zande, J. C. Hone, I. Kymissis, C. R. Kagan, X. Roy and J. S. Owen, Limits of Carrier Diffusion in n-Type and p-Type CH3NH3PbI3 Perovskite Single Crystals, *J. Phys. Chem. Lett.*, 2016, **7**(17), 3510–3518.

83 M. B. Johnston and L. M. Herz, Hybrid Perovskites for Photovoltaics: Charge-Carrier Recombination, Diffusion, and Radiative Efficiencies, *Acc. Chem. Res.*, 2016, **49**(1), 146–154.

84 M. Burgelman, P. Nollet and S. Degrave, Modelling polycrystalline semiconductor solar cells, *Thin Solid Films*, 2000, **361**, 527–532.

85 B. Barman and S. Ingole, Analysis of Si Back-Contact for Chalcogenide Perovskite Solar Cells Based on BaZrS3 Using SCAPS-1D, *Adv. Theor. Simul.*, 2023, **6**(7), 2200820.

86 S. Karthick, S. Velumani and J. Bouclé, Chalcogenide BaZrS3 perovskite solar cells: A numerical simulation and analysis using SCAPS-1D, *Opt. Mater.*, 2022, **126**, 112250.